Process Safety and Environmental Protection 179 (2023) 449–461

Contents lists available at ScienceDirect

Process Safety and Environmental Protection

journal homepage: www.journals.elsevier.com/process-safety-and-environmental-protection

Modelling and optimisation of MXene-derived TiO_2/Ti_3C_2 synthesis parameters using Response Surface Methodology based on the Box–Behnken factorial design. Enhanced carbamazepine degradation by the Cu-modified TiO_2/Ti_3C_2 photocatalyst

Anna Grzegórska [a,*], Jakub Karczewski [b], Anna Zielińska-Jurek [a,*]

[a] Department of Process Engineering and Chemical Technology, Faculty of Chemistry, Gdańsk University of Technology, G. Narutowicza 11/12, 80-233 Gdańsk, Poland
[b] Institute of Nanotechnology and Materials Engineering, Faculty of Applied Physics and Mathematics, Gdańsk University of Technology, G. Narutowicza 11/12, 80-233 Gdańsk, Poland

ARTICLE INFO

Keywords:
Box-Behnken
Carbamazepine
Cu species
MXene
Photocatalysis
Optimisation
RSM
Ti_3C_2
TiO_2

ABSTRACT

In the present study, a hydrothermal method in a water/ethanol environment was used for the first time to obtain novel $Cu/TiO_2/Ti_3C_2$ composites with high photocatalytic activity for the degradation of carbamazepine (CBZ) under simulated solar light. The Box–Behnken factorial design was coupled with Response Surface Methodology (RSM) for synthesis parameter optimisation. The effect of different synthesis parameters, including temperature, time and water/ethanol ratio, was for the first time studied in detail. The analysis of variance (ANOVA) was used to verify the adequacy of the proposed model. The water/ethanol ratio was the most influential parameter for anatase crystallite growth and the efficiency of carbamazepine degradation. The TiO_2/Ti_3C_2 sample prepared under the optimised conditions (synthesis time of 17 h, temperature of 220 °C, and water/ethanol ratio of 58:42 v/v) revealed almost 100% of CBZ degradation within 60 min. Furthermore, the surface modification of this sample with 0.25% - 1 wt% of copper resulted in improved photocatalytic activity. For TiO_2/Ti_3C_2 modified with 0.5% of Cu, almost complete CBZ degradation was observed in 40 min of the photodegradation process. Finally, the combination of the photodegradation process with the activation of peroxymonosulphate (PMS) by $Cu\text{-}TiO_2/Ti_3C_2$ resulted in markedly improved carbamazepine degradation and reached 100% within 20 min under simulated solar light irradiation. The degradation mechanism of CBZ was proposed based on trapping experiments, which revealed that $\bullet O_2^-$ and $\bullet SO_4^-$ are the main oxidising species involved in carbamazepine degradation. Moreover, the hybrid system exhibited high recyclability and stability during subsequent photodegradation cycles.

1. Introduction

The water demand in many places worldwide has surpassed its supply and continues to grow. Population growth, climate change, industrialisation, and destruction of the environment contribute to a greater demand for water (Rathi et al., 2021). Therefore, the recycling of water is crucial. Recently, anthropogenic activities have led to high levels of water resource pollution with emerging contaminants such as endocrine-disrupting compounds, personal care products and pharmaceuticals, which are not biodegradable in conventional wastewater treatment plants. The presence of these substances and their transformation products in aquatic systems may cause serious environmental and health concerns. For example, carbamazepine (CBZ) is the most frequently detected pharmaceutical in water bodies. This antiepileptic drug is a recalcitrant compound that is not susceptible to biodegradation and is not efficiently removed by wastewater treatment plants (WWTPs) or naturally occurring photolysis process. The human body metabolises approximately 72% of CBZ, while 28% is unchanged and subsequently discharged through faeces to the environment, along with its main metabolites, such as 3-hydroxycarbamazepine and carbamazepine-10, 11-epoxide, which are more toxic to daphnids than the parent compound (Zind et al., 2021; Gubitosa et al., 2022). Moreover, it exhibits high water solubility, biomagnification, and bioaccumulation in aquatic organisms. Mezzelani et al. (2020) observed that CBZ was the most

* Corresponding authors.
E-mail addresses: anna.grzegorska@pg.edu.pl (A. Grzegórska), annjurek@pg.edu.pl (A. Zielińska-Jurek).

https://doi.org/10.1016/j.psep.2023.09.028
Received 12 July 2023; Received in revised form 29 August 2023; Accepted 12 September 2023
Available online 16 September 2023
0957-5820/© 2023 The Author(s). Published by Elsevier Ltd on behalf of Institution of Chemical Engineers. This is an open access article under the CC BY license (http://creativecommons.org/licenses/by/4.0/).

frequently detected pharmaceutical in more than 95% of Mediterranean mussels collected over 4 years from 14 sites along the Adriatic and Tyrrhenian Sea. Almeida et al. (2021) reported that CBZ, at environmentally relevant concentrations (up to 1 μg/dm^3), may alter biological responses (physiological, cellular, molecular) in marine bivalves. According to European legislation on the classification and labelling of chemicals (92/32/EEC), carbamazepine is classified as R52/53 substance, which is hazardous to aquatic organisms and may cause long-term adverse effects in the aquatic environment (Zhang et al., 2008). Furthermore, carbamazepine has been proposed as an anthropogenic marker for water bodies. In Germany, CBZ has been detected in WWTPs effluents, surface water, and groundwater at concentrations of 1075–6300 ng·dm^{-3}, 81–1100 ng·dm^{-3}, and 1–100 ng·dm^{-3}, respectively. In the United Kingdom, the concentrations are found to be 152–4596 ng·dm^{-3}, 9–327 ng·dm^{-3}, and 425–3600 ng·dm^{-3} (Hai et al., 2018).

Therefore, the occurrence, fate, transformation, and transfer of the emerging pollutants in the environment must be identified. Moreover, a significant issue to address is the degradation of persistent and emerging contaminants by the application of advanced treatment technologies such as ozonation, Fenton, photo-Fenton, and photocatalysis (Rivera-Utrilla et al., 2013). The selection of a treatment method depends on the specific characteristics of the wastewater and the physicochemical properties of the pharmaceuticals. It is particularly important to consider the potential environmental and human health impacts of each treatment method and select an efficient and sustainable technology.

In this regard, photocatalysis is a significant approach as an efficient green remediation technology for the degradation of persistent and emerging organic pollutants. In this process, the generation of electrons and holes leads to the formation of reactive oxygen species (ROS) such as hydroxyl radicals (OH•), superoxide radical anions ($\bullet O_2^-$), singlet oxygen ($^1O_2$), and hydrogen peroxide (H_2O_2), which can selectively or non-selectively oxidise and mineralise a wide range of contaminants in water and air (Wolski et al., 2019; Afreen et al., 2020). Among a wide group of semiconductor materials, titanium(IV) oxide is a commonly used photocatalyst with low cost, strong oxidising potential, and chemical stability (Simamora et al., 2012). Nevertheless, its activity limited to UV irradiation and fast charge carrier recombination enforces the search for alternative approaches (Dong et al., 2015). The combination of TiO_2 with highly conductive carbonaceous materials is a potential strategy to inhibit the fast recombination of photogenerated electrons and holes (Asencios et al., 2022). Among carbonaceous materials, MXenes have attracted attention in various fields because of their unique properties, including non-toxicity, excellent mechanical strength, large interlayer spacing, extraordinary electrical and thermal conductivity, hydrophilicity, rich surface chemistry, and biocompatibility (Im et al., 2021; Zhang et al., 2020). Moreover, the in situ oxidation of MXene led to the formation of MXene/metal oxide composite, i.e. Ti_3C_2/TiO_2, with intimate contact, which provides highly efficient charge carriers separation (Grzegórska et al., 2021).

In this study, we focused for the first time on the effect of the synthesis parameters, including temperature, time, water/ethanol ratio and modification with copper species on the photocatalytic degradation of carbamazepine in the presence of TiO_2/Ti_3C_2 under simulated solar light. The Box–Behnken factorial design was coupled with Response Surface Methodology (RSM) for optimisation of temperature, water/ethanol ratio, and hydrothermal reaction Then, ANOVA was used to study the statistically significant parameters and their interactions. Furthermore, the TiO_2/Ti_3C_2 sample obtained under optimal conditions was modified with copper species to improve charge carriers separation and enhanced photocatalytic activity under simulated solar light. Among transition metals, copper is an inexpensive metal, almost 100 times and 6000 times cheaper than Ag and Au, with excellent thermal and electrical conductivity (Gawande et al., 2016). Highly reactive copper species can promote various reactions via both one- and two-electron pathways, owing to their wide range of oxidation states

Table 1
Experimental range and levels of the independent variables in the Box–Behnken statistical experimental design.

Variable design	Factors	Coded level		
		-1	0	+ 1
A	Temperature (°C)	180	200	220
B	Time (hours)	6	15	24
C	Amount of ethanol (vol%)	0	50	100

Table 2
The Box-Behnken design with experimental values for the independent variables and optimum conditions determined based on the response optimisation for CBZ degradation.

Experiment symbol	Coded level of variables			Actual level of variables		
	A	B	C	A	B	C
S1	-1	-1	0	180	6	50
S2	+ 1	-1	0	220	6	50
S3	-1	+ 1	0	180	24	50
S4	+ 1	+ 1	0	220	24	50
S5	-1	0	-1	180	15	0
S6	+ 1	0	-1	220	15	0
S7	-1	0	+ 1	180	15	100
S8	+ 1	0	+ 1	220	15	100
S9	0	-1	-1	200	6	0
S10	0	+ 1	-1	200	24	0
S11	0	-1	+ 1	200	6	100
S12	0	+ 1	+ 1	200	24	100
S13	0	0	0	200	15	50
S14	0	0	0	200	15	50
S15	0	0	0	200	15	50
S16	optimum conditions			220	17	42

(Cu^0, Cu^+, Cu^{2+}, and Cu^{3+}) (Muscetta et al., 2020).

In addition, copper species may effectively activate peroxymonosulphate (PMS) to produce sulphate radicals, a promising alternative to hydroxyl radicals. The $\bullet SO_4^-$ radicals have a higher redox potential (E_0 = 2.5–3.1 V) than OH• (1.8–2.8 V) radicals. Moreover, sulphate radicals reveal a longer half-life (4×10^{-5} s) than that of OH• radicals (2×10^{-5} s). Notably, during $\bullet SO_4^-$ based oxidation processes, secondary oxidants such as •OH, $\bullet O_2^-$, and $^1O_2$ can also be produced, which accelerates the degradation rate of organic contaminants (Hasija et al., 2022). Therefore, a promising strategy of photocatalysis assisted by peroxymonosulphate (PMS) activation for enhanced CBZ degradation is proposed in this study.

2. Materials

Ti_3AlC_2 was purchased from Luoyang Tongrun Info Technology Co. (China). HF (ACS reagent, 50%), ethanol (anhydrous, 99.8%), copper (II) nitrate trihydrate (p.a., 99–104%), potassium peroxymonosulphate (OXONE, monopersulphate compound), and carbamazepine (Pharmaceutical Secondary Standard; Certified Reference Material) were provided by Sigma Aldrich. Beznoquinone (reagent grade, ≥ 98%), ammonium oxalate (ACS reagent, ≥ 99%), isopropanol (anhydrous, 99.5%), and tert-butanol (anhydrous, 99.5%) were supplied by Sigma Aldrich. Acetonitrile (HPLC grade) and H_3PO_4 (85%, HPLC grade) applied to determine the CBZ concentration by HPLC were provided by Sigma Aldrich. All reagents were used as received without additional treatment. Deionised (DI) water was used in all experiments.

3. Methods

3.1. Experiment design

The statistical software Minitab version 21.1 (Minitab USA, 2021) was used to design and analyse the effects of various synthesis

MOST WIEDZY Downloaded from mostwiedzy.pl

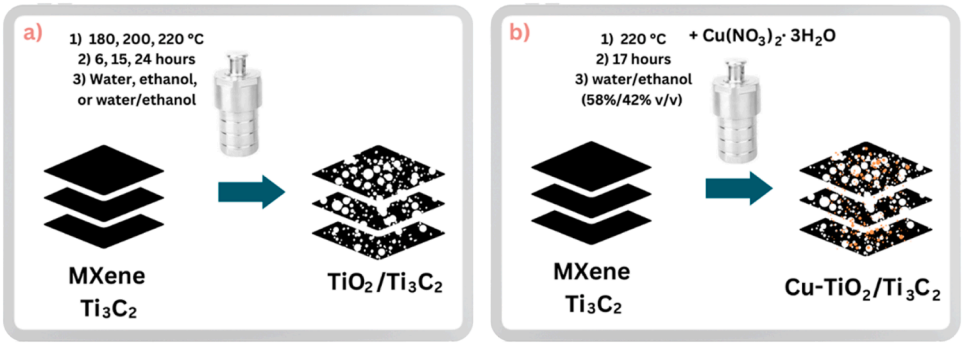

Fig. 1. Schematic representation of the synthesis procedure.

parameters on the physicochemical properties of the materials and the photodegradation of CBZ. A three-factor three-level Box-Behnken experimental design (BBD), along with RSM, was used to correlate the interactions among the variables and responses. Based on the BBD design, 15 runs were performed to obtain precise results. The coefficients were analysed using analysis of variance (ANOVA). Each of the parameters was analysed on the three levels: low (−1), high (+1), and centre point (0). Table 1. represents the levels and ranges of the selected independent variables. The Box-Behnken experimental design, with three independent variables, is presented in Table 2.

3.2. Preparation of MXene – $Ti_3C_2T_x$

First, 10 g of Ti_3AlC_2 was gradually added to 100 cm^3 of HF. The suspension was mixed for 24 h at room temperature. The sample was then centrifuged and washed with DI water until the pH of the washing solution was neutral.

3.3. Synthesis of TiO_2/Ti_3C_2 composite

In a typical procedure, 0.4 g $Ti_3C_2T_x$ was dispersed in water (60 cm^3), a water-ethanol mixture (1:1 v/v), or ethanol. The mixture was sonicated for 10 min to obtain a homogeneous dispersion and then mixed for another 30 min. The suspension was transferred to a Teflon-lined stainless-steel autoclave reactor and held in an oven for 6, 15, or 24 h at 180, 200, or 220 °C, according to the parameters summarised in Tables 1 and 2.

3.4. Preparation of Cu-deposited TiO_2/Ti_3C_2 composites

The TiO_2/Ti_3C_2 composites were modified with Cu particles using the one-pot synthesis method, as presented in Fig. 1. In the first step, 0.4 g $Ti_3C_2T_x$ was dispersed in 60 cm^3 of a water/ethanol mixture (58:42 v/v). Then, a proper volume of $Cu(NO_3)_2{\cdot}3\ H_2O$ aqueous solution corresponding to 0.25 wt%, 0.5 wt% and 1 wt% of Cu was added. Next, the sample was sonicated for 10 min and mixed for 30 min. The suspension was transferred to a Teflon-lined stainless steel autoclave reactor and held in an oven for 17 h at 220 °C.

3.5. Characterisation methods

The prepared materials were characterised using X-ray powder diffraction (XRD). This technique was used to determine the composition of the prepared photocatalysts and the crystallite size. XRD patterns were obtained with a powder diffractometer Rigaku Intelligent X-ray diffraction system SmartLab (Rigaku Corporation, Tokyo, Japan) with Cu Kα radiation, and in the 2θ range from 5° to 80°, with a speed of 2°min^{-1} and a step of 0.01°. UV–vis reflectance spectra of the powdered photocatalysts were recorded using a Thermo Scientific Evolution 220 spectrophotometer (Waltham, MA, USA). $BaSO_4$ was used as the reference material. Absorbance was recorded in the wavelength range of 200–800 nm. The Brunauer-Emmett-Teller (BET) surface area was determined using a Micromeritics Gemini V analyser (Norcross, GA, USA) in liquid nitrogen. Before the measurements, the powder samples (approximately 0.1 g) were degassed at 200 °C for 2 h under constant nitrogen flow. Scanning electron microscopy (SEM) was used to determine the morphologies of the prepared composites. The SEM images were obtained using an SEM microscope (FEI Quanta FEG 250). Transmission electron microscopy (TEM) analyses were conducted using a Thermo Fisher (formerly FEI) Titan Themis G2 200 Probe Cs Corrected Scanning Transmission Electron Microscope (STEM). Photoluminescence (PL) spectra were recorded on a spectrofluorometer Shimadzu RF-6000 (Kyoto, Japan). A 150 W Xenon lamp with an excitation wavelength of 300 nm was used as the excitation source. XPS analyses were performed using a multi-chamber UHV PREVAC system. The photoelectron excitation source was an X-ray tube VG Scienta SAX 100 with an aluminum anode equipped with a monochromator VG Scienta XM 780, emitting radiation with the characteristic line of Al Kα and an energy of 1486.6 eV. Spectral deconvolution was performed using CasaXPS Version 2.3.25 PR1. Electrochemical measurements were performed using an Autolab Potentiostat/Galvanostat Autolab (model PGSTAT204). The photocatalytic materials were placed on carbon screen-printed electrodes with an Ag reference electrode. The electrolyte solution (0.5 M Na_2SO_4) was purged with Ar for 10 min prior to the measurements. Electrochemical impedance spectra (EIS) Nyquist plots were recorded in the range of 10^5 Hz to 0.1 Hz with an AC voltage amplitude of 0.01 V. Mott Schottky plots were registered for the applied frequency of 1000 Hz in the potential range from − 1.5–0 V. The transient photocurrent response of the photocatalysts was recorded at a light on/off interval of 25 s at 0 V vs. Ag under 372 nm LED light illumination.

3.6. Photocatalytic activity

In a typical procedure, a photocatalyst suspension (2 g/dm^3) was prepared in a carbamazepine solution (14 mg/dm^3) in a 25 cm^3 glass reactor with a quartz window. The suspension was aerated throughout the experiment. Prior to photodegradation, the suspension was mixed in the dark for 30 min to achieve adsorption-desorption equilibrium. Subsequently, the photocatalytic experiment was performed using a 300 W Xenon lamp emitting simulated solar light irradiation. The spectrum of the used Xe lamp is presented in Fig. S1 in Supporting Materials. The reaction temperature was maintained at 20 °C. The samples were collected at 0, 20, 40, and 60 min of the process. Furthermore, the photocatalyst was separated from the solution using a 0.2 μm syringe filter. The progress of pollutant photodegradation was analysed using reverse-phase high-performance liquid chromatography (HPLC) (Shimadzu UFLC LC-20AD (Kyoto, Japan) with a photodiode array detector (Shimadzu SPD-M20A). Measurements were performed at 45 °C under isocratic flow conditions of 1.5 $cm^3{\cdot}min^{-1}$. The volume

MOST WIEDZY Downloaded from mostwiedzy.pl

Table 3
Box-Behnken experimental results: carbamazepine degradation (%), TOC removal (%), specific surface area (m^2/g), and average anatase crystallite size (nm) of anatase TiO_2 particles.

Sample no.	Sample label	BET surface area (m^2/g)	Anatase crystallite size (nm)	Efficiency of degradation (%)	Degradation rate constant ($min^{-1} \cdot 10^{-2}$)	TOC removal (%)
S1	T180/EtOH-H_2O/6 h	34.1	12	66	1.84 ± 0.09	9.2
S2	T220/EtOH-H_2O/6 h	42.6	13.5	83	2.93 ± 0.12	16.4
S3	T180/EtOH-H_2O/ 24 h	38.1	13	88	3.54 ± 0.05	18.3
S4	T220/EtOH-H_2O/ 24 h	50.6	17	95	4.86 ± 0.07	21.2
S5	T180/H_2O/15 h	24.3	18	57	1.46 ± 0.06	3.7
S6	T220/H_2O/15 h	29.1	24	84	2.77 ± 0.08	11.0
S7	T180/EtOH/15 h	57.6	13	48	1.11 ± 0.05	9.2
S8	T220/EtOH/15 h	33.2	15	83	2.68 ± 0.09	12.8
S9	T200/H_2O/6 h	37.2	19	79.5	2.57 ± 0.04	7.3
S10	T200/H_2O/24 h	30.3	25	81	2.63 ± 0.05	17.3
S11	T200/EtOH/15 h	42.9	11.5	50	1.19 ± 0.07	10.1
S12	T200/EtOH/24 h	69.6	13	52	1.28 ± 0.03	13.5
S13	T200/EtOH-H_2O/ 15 h	38.3	13	97	5.34 ± 0.09	22.4
S14	T200/EtOH-H_2O/ 15 h	42.4	13	96.5	5.21 ± 0.13	22.9
S15	T200/EtOH-H_2O/ 15 h	39.5	13	97	5.39 ± 0.11	23.8
S16	T220/EtOH-H_2O/ 17 h	38.2	18	99.5	6.56 ± 0.13	25.2

composition of the mobile phase was 39.5% acetonitrile, 60% water, and 0.5% orthophosphoric acid. Determination of CBZ concentration was performed using the C18 column, with the injection volume of 10 µL, and the detection wavelength was set at 285 nm. The mean retention time of CBZ was 4.6 min. The calibration curve for the determination of CBZ concentration is presented in Fig. S2 in Supporting Materials.

For the photodegradation process coupled with PMS activation, after reaching the adsorption-desorption equilibrium, 0.5 mM of PMS was added to the photoreactor. The samples were collected at 0, 5, 10, 20, 30, 40, and 60 min of the process. Subsequently, after photocatalyst separation, 200 µL of methanol was added to each sample to quench the generated radical species.

Furthermore, trapping experiments were performed to analyse the mechanism of the CBZ degradation. Benzoquinone was used as a superoxide anion radicals scavenger, ammonium oxalate as holes scavenger, isopropanol as a hydroxyl radicals and sulphate radicals scavenger, and tert-butanol as a hydroxyl radicals scavenger. The concentration of the scavengers was 10-times higher than that of the CBZ in the solution.

4. Results and discussion

4.1. Box–Behnken design (BBD) and characteristic of TiO_2/Ti_3C_2 composites

Firstly, a three-factor three-level Box-Benkhen design (BBD) was developed to optimise the synthesis parameters and describe the photocatalytic degradation of carbamazepine in an aqueous solution. Carbamazepine is a persistent pharmaceutical compound not susceptible to biodegradation. Therefore, in this study, we investigated the effect of photocatalyst synthesis parameters on carbamazepine degradation to propose a highly efficient advanced treatment process.

The results obtained from the 15 experiments planned using the BBD are presented in Table 3. The responses were the efficiency of carbamazepine degradation (%), TOC removal efficiency (%), BET-specific surface area (m^2/g), and average anatase crystallite size (nm). According to the results presented in Table 3, polynomial equations in an uncoded form showing the empirical relationship between the responses (CBZ degradation, TOC removal, BET surface area, and crystallite size) and independent variables were determined.

The surface area of a photocatalyst is an important factor affecting the efficiency of the photocatalytic degradation process. A higher specific surface area with more reactive sites and a shorter migration distance may reduce the recombination rate of photogenerated electron-hole pairs (Isac et al., 2022). Furthermore, materials with higher surface areas exhibit better adsorption properties (Danish et al., 2021).

The polynomial equation representing the empirical relationship between the BET surface area and the independent variables is shown in Eq. 1. The coefficient of determination (R^2) of the model was 0.88.

$$BET\ surface\ area\ (m^2/g) = -400 + 4{\cdot}23{\cdot}A - 3{\cdot}55{\cdot}B + 1{\cdot}386{\cdot}C - 0{\cdot}00984{\cdot}A^2 + 0{\cdot}0643{\cdot}B^2 - 0{\cdot}00004{\cdot}C^2 + 0{\cdot}0055{\cdot}A{\cdot}B - 0{\cdot}00731{\cdot}A{\cdot}C + 0{\cdot}01902{\cdot}B{\cdot}C \quad (1)$$

The highest surface areas of 50.6 $m^2{\cdot}g^{-1}$, 57.6 $m^2{\cdot}g^{-1}$, and 69.6 $m^2{\cdot}g^{-1}$ were noticed for samples S4 (T220/EtOH-H_2O/24 h), S7 (T180/EtOH/15 h) and S12 (T200/EtOH/24 h), respectively. By analysing the 3D surface plots presented in Fig. 2, an increase in the BET surface area with an increase in the synthesis time and amount of ethanol used as a reaction medium was observed. The BET surface area increased with an increase in the hydrothermal reaction temperature to 200 °C, and decreased above this temperature. The ANOVA results and Pareto chart in Table S1 and Fig. S3 in the Supporting Materials show that the amount of ethanol (C) had the highest influence on the BET surface area. Only for this variable, the p-value was lower than the significance level ($p \leq \alpha$), and exceeded the red vertical line (2.571) in the Pareto chart.

Crystallite size is also one of the parameters involved in controlling photocatalytic activity. The crystallite size was calculated based on the XRD analyses presented in Fig. S4 in Supporting Materials. For all the obtained samples (S1-S15), the characteristic signals for both the anatase and MXene phases were identified. The main signals at 8.9°, 18.3°, 27.6°, and 60.6° were assigned to the (002), (004), (006), and (110) planes of MXene, respectively, and at 25.3°, 48.0°, 53.8°, and 55.0° to the (101), (200), (105), and (211) planes of anatase, respectively. The largest anatase crystallite size was observed for the samples prepared in water as a reaction medium (S5, S6, and S10) and the smallest was obtained with the addition of ethanol, which enabled the control of anatase particle nucleation and growth (samples S1, S7, and S11) (Dudziak et al., 2021).

The polynomial equation representing the empirical relationship

MOST WIEDZY Downloaded from mostwiedzy.pl

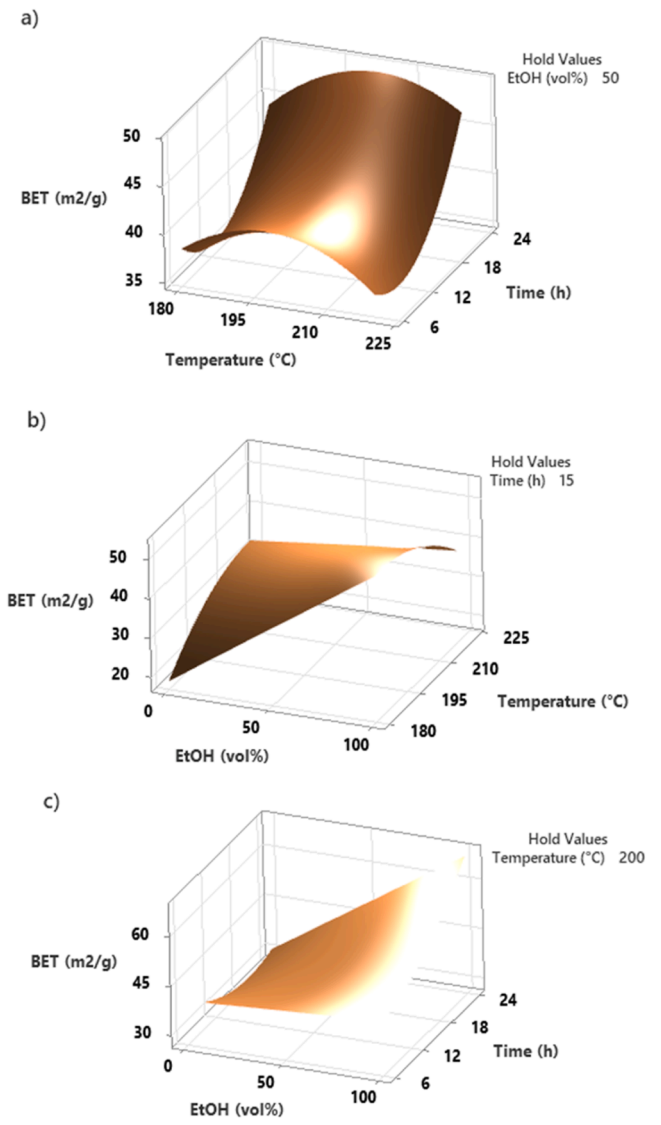

Fig. 2. 3D surface plots showing the effects of (a) temperature and synthesis time, (b) amount of ethanol and temperature, and (c) amount of ethanol and synthesis time on the BET surface area development.

between the anatase crystallite size and the independent variables is shown in Eq. 2.

The coefficient of determination (R^2) of the model was 0.98. ANOVA results and a Pareto chart (Table S2 and Fig. S5 in the Supporting Materials) showed that the amount of ethanol (C and C^2), temperature (A), and time (B) had the highest impact on the crystallite size.

$$\textit{Crystallite size (nm)} = 44{\cdot}8 - 0{\cdot}369{\cdot}A - 0{\cdot}262{\cdot}B + 0{\cdot}017{\cdot}C + 0{\cdot}00116{\cdot}A^2 + 0{\cdot}00015{\cdot}B^2 + 0{\cdot}001535{\cdot}C^2 + 0{\cdot}00264{\cdot}A{\cdot}B - 0{\cdot}001100{\cdot}A{\cdot}C - 0{\cdot}00233{\cdot}B{\cdot}C \quad (2)$$

As presented in Fig. 3, the average anatase crystallite size was positively correlated with the hydrothermal reaction temperature, time, and ethanol concentration. It was found that a longer time and higher temperature facilitated the anatase grain growth. In contrast, the average crystallite size decreased with increasing ethanol concentration. The presence of ethanol suppressed the hydrothermal oxidation of $Ti_3C_2T_x$. Furthermore, according to Zhang et al. (2017), without ethanol, TiO_2 nuclei readily grow into TiO_2 grains because of complete contact with water. Furthermore, the presence of ethyl alcohol resulted in steric hindrance, limiting grain growth and leading to the formation of smaller anatase nanoparticles.

The DR/UV–vis spectra of the selected TiO_2/Ti_3C_2 composites are

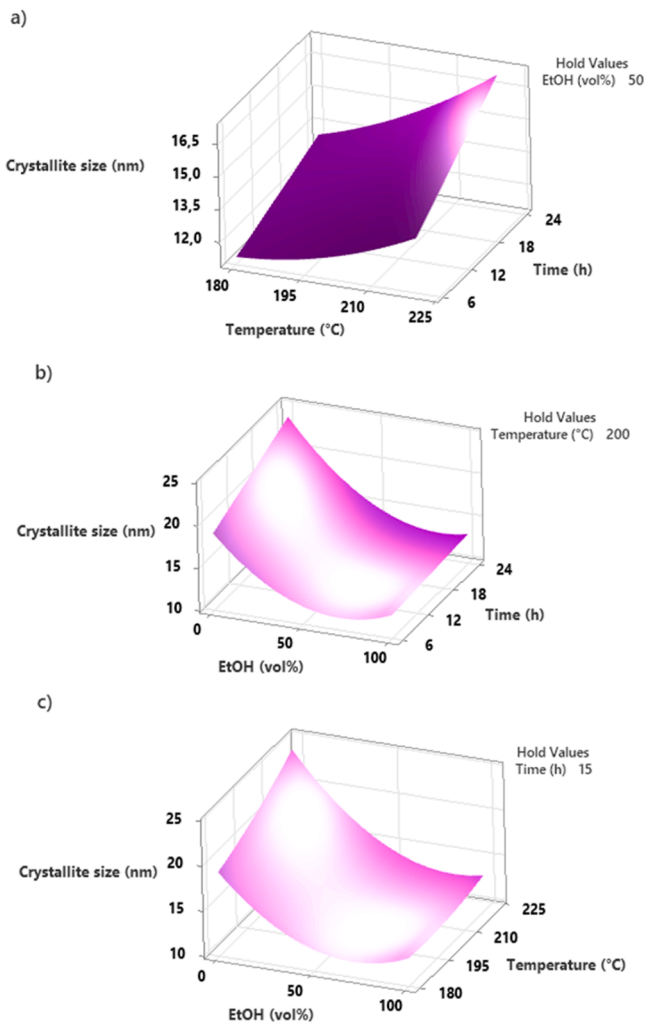

Fig. 3. 3D surface plots presenting the effects of (a) temperature and synthesis time, (b) amount of ethanol and temperature, and (c) amount of ethanol and synthesis time on TiO_2 crystallite size.

presented in Fig. S6 in Supporting Materials. All samples showed a characteristic absorption band for TiO_2 in the range of 200–350 nm. The significant increase in the absorption in the range of 400–800 nm may be attributed to the presence of MXene and its full-spectrum absorption.

Finally, scanning electron microscopy (SEM) images of the TiO_2/Ti_3C_2 composites synthesised under different conditions are shown in Fig. 4. The layered structure of MXene was preserved after the solvothermal treatment. The MXene surface was uniformly covered with fine TiO_2 nanoparticles. Furthermore, increasing the synthesis temperature led to complete coverage of the MXene sheets with the TiO_2 agglomerates.

The polynomial equation representing the empirical relationship between CBZ degradation (%) and the independent variables is presented in Eq. 3. The coefficient of determination (R^2) of the model was 0.87.

$$\textit{CBZ degradation (\%)} = -667 + 6{\cdot}56{\cdot}A + 6{\cdot}32{\cdot}B + 0{\cdot}29{\cdot}C - 0{\cdot}0148{\cdot}A^2 - 0{\cdot}10001{\cdot}B^2 - 0{\cdot}00933{\cdot}C^2 - 0{\cdot}0142{\cdot}A{\cdot}B - 0{\cdot}00231{\cdot}A{\cdot}C + 0{\cdot}0004{\cdot}B{\cdot}C \quad (3)$$

By analysing the 3D surface plots (Fig. 5), it can be observed that the efficiency of CBZ degradation increased with an increase in the synthesis temperature. An opposite effect was observed for the amount of ethanol in the reaction environment. The addition of ethanol improved the photocatalytic activity; however, above the optimal amount of ethanol, the degradation efficiency decreased. Based on 15 experiments, the

MOST WIEDZY Downloaded from mostwiedzy.pl

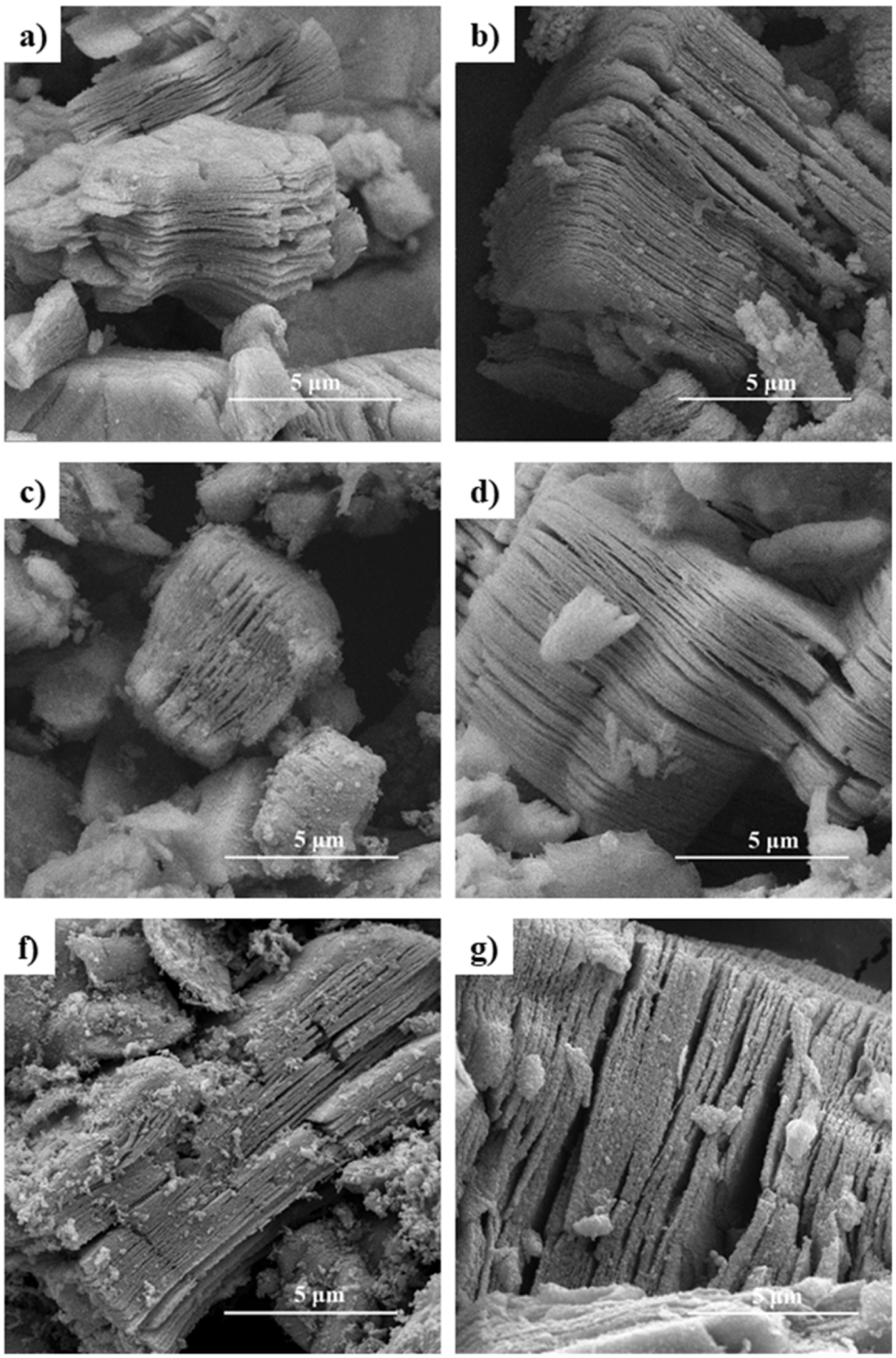

Fig. 4. SEM images of S13 (T200/EtOH-H_2O/15 h) (a), S10 (T200/H_2O/24 h) (b), S4 (T220/EtOH-H_2O/24 h) (c), S12 (T200/EtOH/24 h) (e), S16 (T220/EtOH-H_2O/17 h) (f), and 0.5% Cu-S16 (Cu-modified T220/EtOH-H_2O/17 h) (g).

highest photocatalytic activity towards CBZ degradation was observed for sample S15 (T200/EtOH-H_2O/15 h), synthesised at 200 °C for 15 h with an ethanol/water ratio of 50:50 v/v. The degradation of CBZ reached 97% within 60 min under simulated solar light irradiation. ANOVA results and Pareto chart (Table S3 and Fig. S7 in the Supporting Materials) showed that the amount of ethanol (C^2) and temperature (A) had the highest impact on the photocatalytic CBZ degradation. Only for these two variables, the p-value was lower than the significance level ($p \leq \alpha$) and exceeded the red vertical line, indicating a minimum statistically significant effect (2.571) in the Pareto chart.

To further improve CBZ degradation, optimisation of the response was performed, and the synthesis parameters were predicted to be 220 °C, 17 h, and a water–ethanol mixture with a ratio of 58:42 v/v. Furthermore, to confirm the predictions, the photocatalyst was synthesised under these conditions. The photocatalytic activity experiment confirmed that the degradation was the highest among all analysed samples for this composite, reaching nearly 100% within 60 min of irradiation.

MOST WIEDZY Downloaded from mostwiedzy.pl

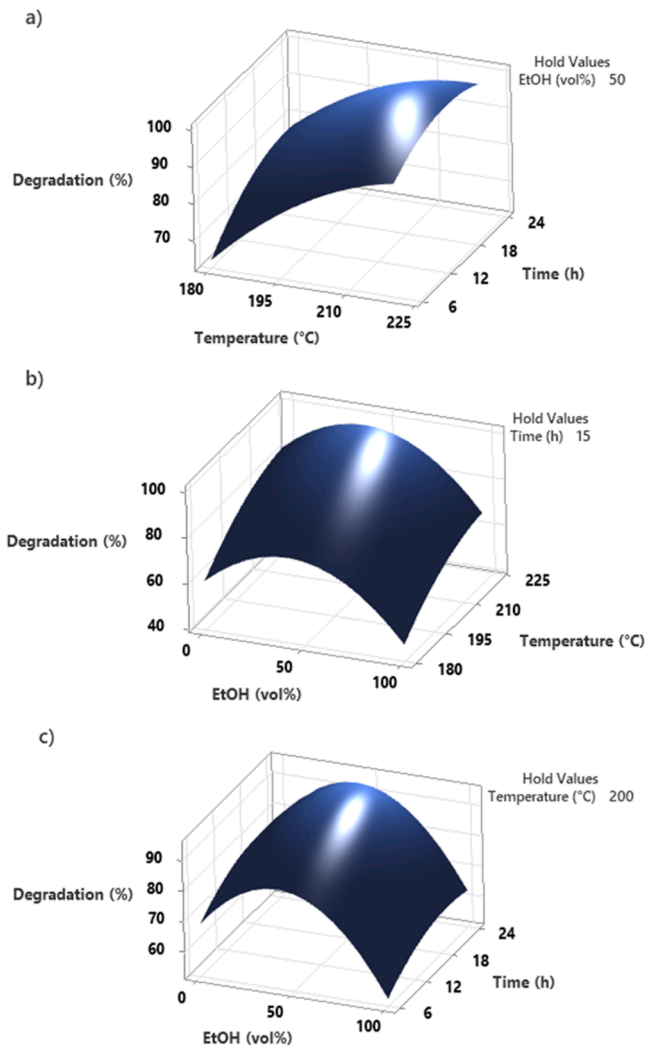

Fig. 5. 3D surface plots presenting the effects of (a) temperature and synthesis time, (b) amount of ethanol and temperature, and (c) amount of ethanol and synthesis time on CBZ degradation (%).

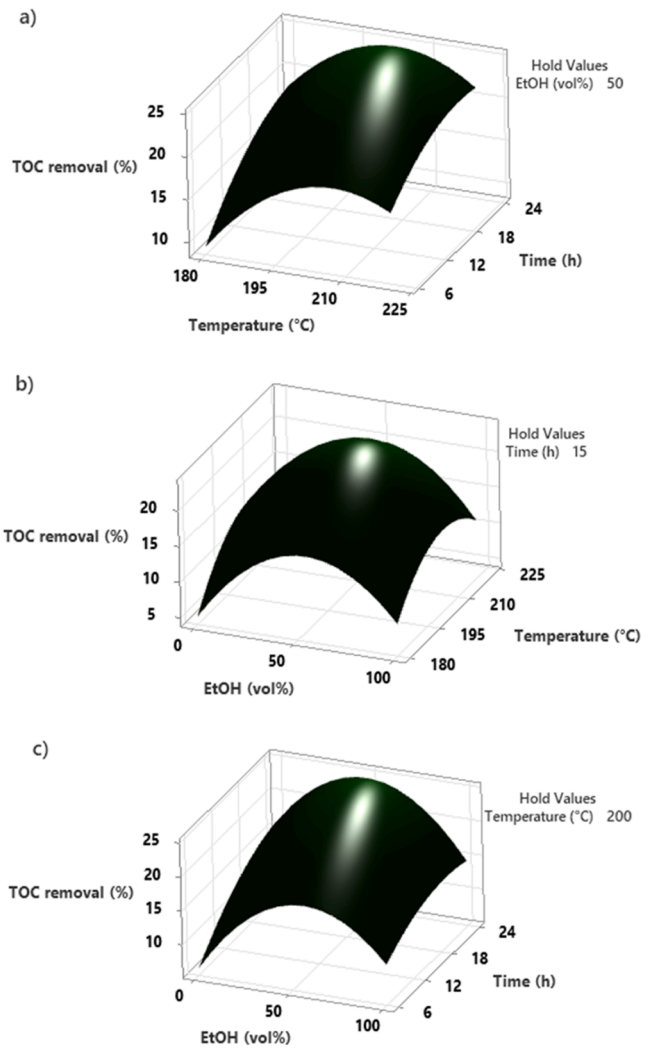

Fig. 6. 3D surface plots presenting the effects of (a) temperature and synthesis time, (b) amount of ethanol and temperature, and (c) amount of ethanol and synthesis time on TOC removal.

The progress in the photodegradation process also reflects the mineralisation of organic compounds to CO_2 and H_2O. This process may be evaluated by the determination of the total organic carbon (TOC) removal after the degradation process. The polynomial equation representing the empirical relationship between TOC removal after the photocatalytic process (%) and the independent variables is shown in Eq. 4. The coefficient of determination (R^2) of the model was 0.98.

$$TOC\ removal\ (\%) = -535{\cdot}7 + 5{\cdot}084{\cdot}A + 2{\cdot}467{\cdot}B + 0{\cdot}617{\cdot}C - 0{\cdot}01204{\cdot}A^2 - 0{\cdot}02397{\cdot}B^2 - 0{\cdot}003617{\cdot}C^2 - 0{\cdot}00597{\cdot}A{\cdot}B - 0{\cdot}000925{\cdot}C - 0{\cdot}00367{\cdot}B{\cdot}C \quad (4)$$

Based on the 3D surface plots presented in Fig. 6, it can be observed that the reduction in TOC concentration, similar to the photocatalytic activity, increased with increasing synthesis temperature and time.

The amount of ethanol in the synthesis above the optimal value caused a decrease in TOC removal after the photocatalytic process. The ANOVA results and Pareto chart (Table S4 and Fig. S8 in Supporting Materials) showed that the amount of ethanol (C^2) had the greatest influence on TOC removal, followed by synthesis time, and temperature. For these variables, the p-value was lower than the significance level ($p \leq \alpha$) and exceeded the red vertical line (2.571) in the Pareto chart.

Table 4
The anatase crystallite size, BET surface area, and band gap energy for Cu-S16 composites.

Sample	Crystallite size (nm)	BET surface area (m^2/g)	Band gap (eV)
0.25% Cu-S16	19	41.2	3.13
0.5% Cu-S16	17	40.9	3.10
1% Cu-S16	17	40.3	3.09

4.2. Characterisation of Cu-modified TiO_2/Ti_3C_2 composites

In the next step, the sample synthesised under optimised conditions (sample S16 with a synthesis time of 17 h, temperature of 220 °C, and water/ethanol ratio of 58:42 v/v) was modified with different amounts of Cu in the range from 0.25 wt% to 1 wt%.

The BET surface areas of the composite materials in the series Cu-S16 were similar and equalled 40–41 $m^2{\cdot}g^{-1}$, slightly higher than that of pure S16 sample (38.2 m^2/g). The band gap energy of the S16 composite was 3.14 eV, and similar values (Table 4) were obtained for Cu-modified samples, as presented in Table 4.

Based on the XRD analysis, only the signals corresponding to TiO_2 and Ti_3C_2 were noticed, as presented in Fig. 7. Any copper species were

MOST WIEDZY Downloaded from mostwiedzy.pl

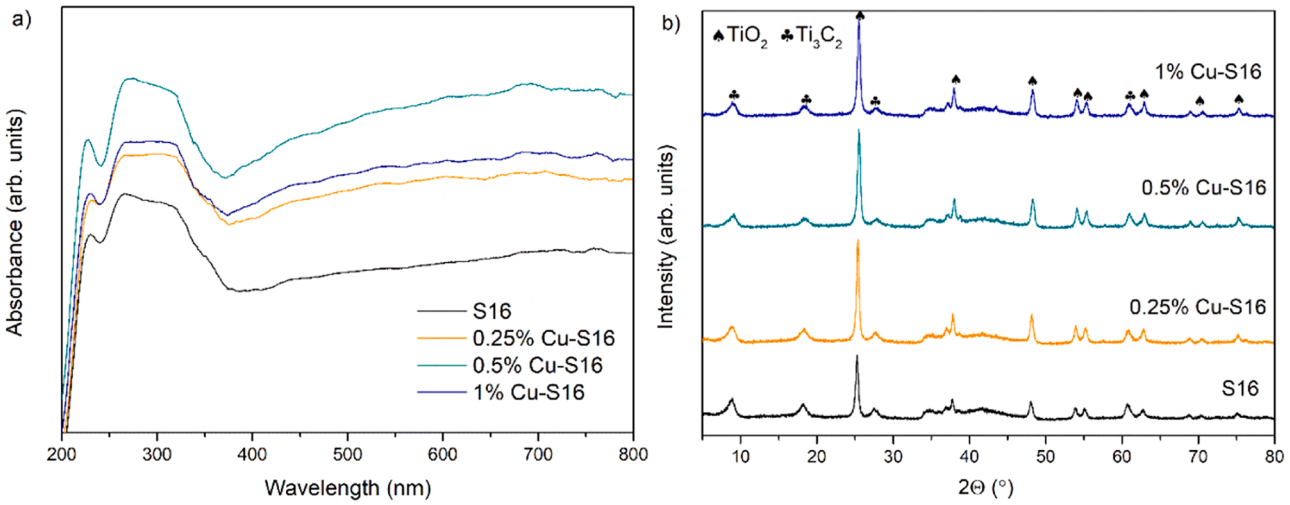

Fig. 7. DR/UV–vis spectra (a) and XRD diffractograms (b) of the S16 (T220/EtOH-H_2O/17 h) and Cu-modified T220/EtOH-H_2O/17 h samples with different amounts of copper.

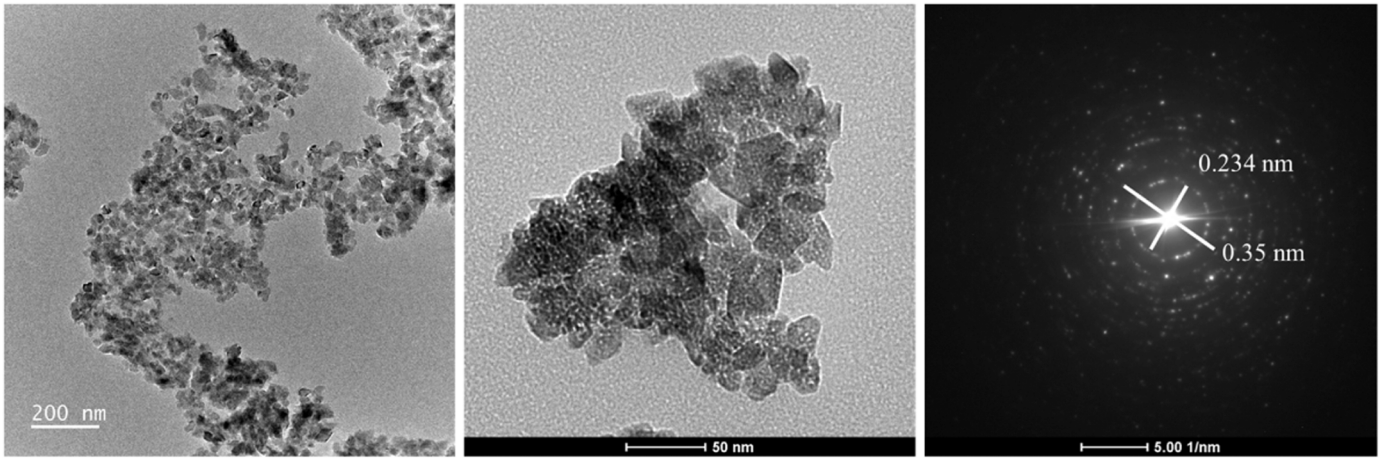

Fig. 8. TEM images and SAED pattern of 0.5% Cu-S16 sample.

detected in the composite materials. It may be related to the low amount of Cu in the composite structure or suggests that copper was uniformly distributed on the TiO_2/Ti_3C_2 surface. Because the radius of Cu^{2+} (0.087 nm) is considerably larger than that of Ti^{4+} (0.0745 nm) and there is a large difference in the valence state, copper should not replace titanium in the crystal lattice (Yan et al., 2015).

Furthermore, SEM-EDS analysis confirmed the presence of copper on the Ti_3C_2/TiO_2 composite surface, as shown in Fig. S9 in the Supporting Materials. The copper content for the 0.5% Cu-S16 sample was about 0.51 wt% (0.19 at%), which is consistent with the amount used for modification. TEM images are presented in Fig. 8. The formation of small TiO_2 nanoparticles on the MXene surface was visible. Based on the TEM with the corresponding SAED pattern, d-spacing values equalled 0.35 nm and 0.234 nm were ascribed to the anatase (101) and $Ti_3C_2T_x$ (103) planes, respectively (Verma et al., 2017; Huang et al., 2022).

XPS analysis was performed to identify the oxidation states of the elements and are presented in Fig. 9. The Ti 2p $_{3/2}$ components at 455.2 eV, 456.5 eV, 457.9 eV, and 459.5 eV correspond to Ti bound to C, Ti(II), Ti(III) and Ti(IV), respectively (Zhu et al., 2016). For the O 1 s region, peaks at 530.7 eV and 532.3 eV are ascribed to Ti–O–Ti in TiO_2 and Ti-OH, respectively. The OH terminates on the surface of Ti_3C_2 (Ding et al., 2019). The C 1 s spectrum was deconvoluted into nine peaks fitted at 282 eV, 284.4 eV, 285 eV, 285.6 eV, 286.2 eV, 287 eV, 287.9 eV, 289.1 eV, and 289.8 eV. These peaks were assigned to the Ti-C, C═C, C-H, C-C, C-OH, C-O-C, C═O, C-F, and O═C-O bonds, respectively (Ahmed et al., 2016; Kalambate et al., 2020). XPS analysis revealed the presence of copper (0.1 at%) in the composite material. The peak was deconvoluted for two signals at 932.3 eV and 934.1 eV corresponding to Cu(0) and/or Cu(I), and Cu(II), respectively. Only based on the XPS spectrum in the Cu 2p region, it is difficult to distinguish between metallic Cu and Cu(I) due to the similar BE values (Biesinger et al., 2010; Shaaban and Li, 2022). The prevailing quantity of Cu(0)/Cu (I) over Cu(II) indicates the partial self-reduction of copper on the MXene surface without an external reducing agent. This phenomenon occurs due to the strong reductive activity of low-valence Ti(II) and Ti (III) species and the presence of negatively charged terminal groups (Wang et al., 2023; Zou et al., 2016). Similarly, a self-reduction process on the $Ti_3C_2T_x$ surface was observed for Ag, Au, Ni, and Cu (Li et al., 2022; Zhou et al., 2022; Zhang et al., 2016; Li et al., 2018).

The photoluminescence spectra are presented in Fig. 10. The spectra show a broad band between 400 and 650 nm, with a maximum photoluminescence intensity at 460 nm. The incorporation of copper into the composite material led to a decrease in photoluminescence. Furthermore, the highest decrease was observed for the 0.5% Cu-S16 sample, possibly due to the lowest recombination of photoexcited charge carriers, thus improving photocatalytic efficiency. Meanwhile, for the sample modified with 1% of copper, the PL peak intensity was stronger than that of the sample modified with 0.5% of copper, indicating that an

MOST WIEDZY Downloaded from mostwiedzy.pl

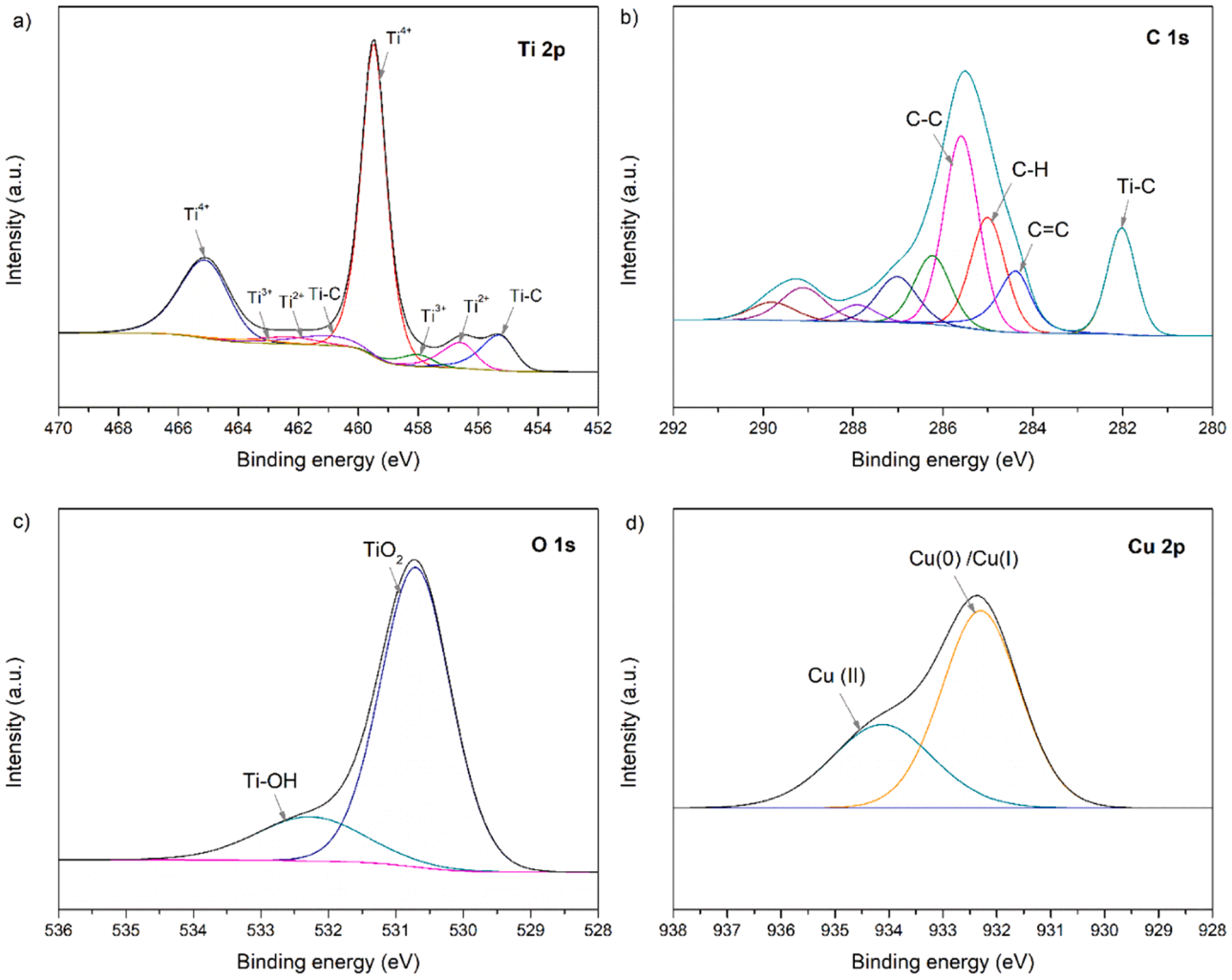

Fig. 9. XPS spectra of Ti 2p (a), C 1 s (b), O 1 s (c), and Cu 2p (d) regions for sample 0.5% Cu-S16.

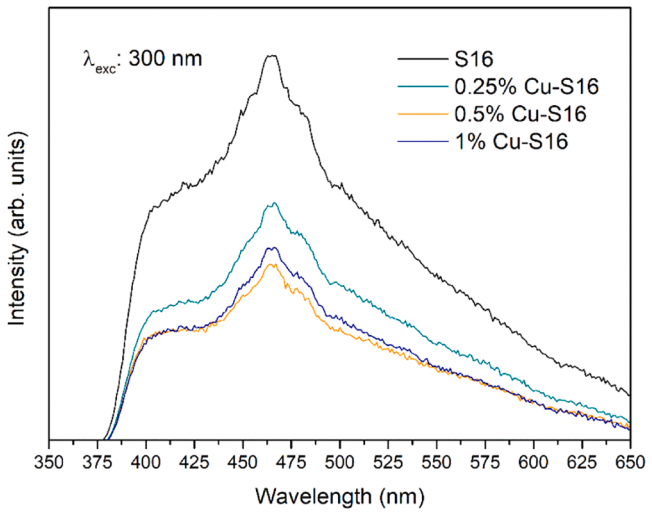

Fig. 10. Photoluminescence spectra of Cu-modified composite materials.

excessive amount of Cu negatively affected the charge carriers separation. Excessive Cu agglomerates can form new recombination centres for photogenerated charge carriers.

Electrochemical impedance spectroscopy is a suitable method to characterise the charge transfer resistance. The EIS Nyquist plots of the prepared materials are presented in Fig. 11a. The diameter of the semicircle in the EIS Nyquist plot correlates with the charge transfer resistance and separation efficiency of the photogenerated electron-hole pairs at the interface between the material and the electrolyte solution. It can be seen that the 0.5% Cu-S16 sample showed the smallest impedance arc radius compared with the other Cu-modified samples and pure TiO_2/Ti_3C_2. This is related to the excellent electronic conductivity of Cu, and enhancement in the Cu-modified composite conductivity compared to pure TiO_2/Ti_3C_2. The direct contact between deposited Cu species and TiO_2/Ti_3C_2 results in efficient photogenerated charge carriers separation, faster and easier electron transfer and lower electron-hole recombination rate (Vattikuti et al., 2018). Similar effect was also confirmed in previous studies for Cu-TiO_2 (Hua et al., 2016) and Cu-$BiVO_4$ (Wu et al., 2022). A lower resistance is correlated with a higher photocurrent response for samples modified with copper. For both samples, a photocurrent was instantly generated once the light was turned on. The photocurrent response of the composite modified with copper was improved compared to TiO_2/Ti_3C_2 sample (Fig. 11b). The photocurrent density for 0.5% Cu-S16 was 12.76 μA/cm^2, while for S16 was 3.46 μA/cm^2, which was above 3.5 times greater for copper-modified TiO_2/Ti_3C_2. The higher the photocurrent, the higher is the charge carriers separation efficiency (Shen et al., 2018). In the five-cycle measurement, similar photocurrent values were obtained for each switch on/off cycle, showing the excellent reproducibility of the materials. According to the Mott Schottky plot (Fig. 12), the conduction

MOST WIEDZY Downloaded from mostwiedzy.pl

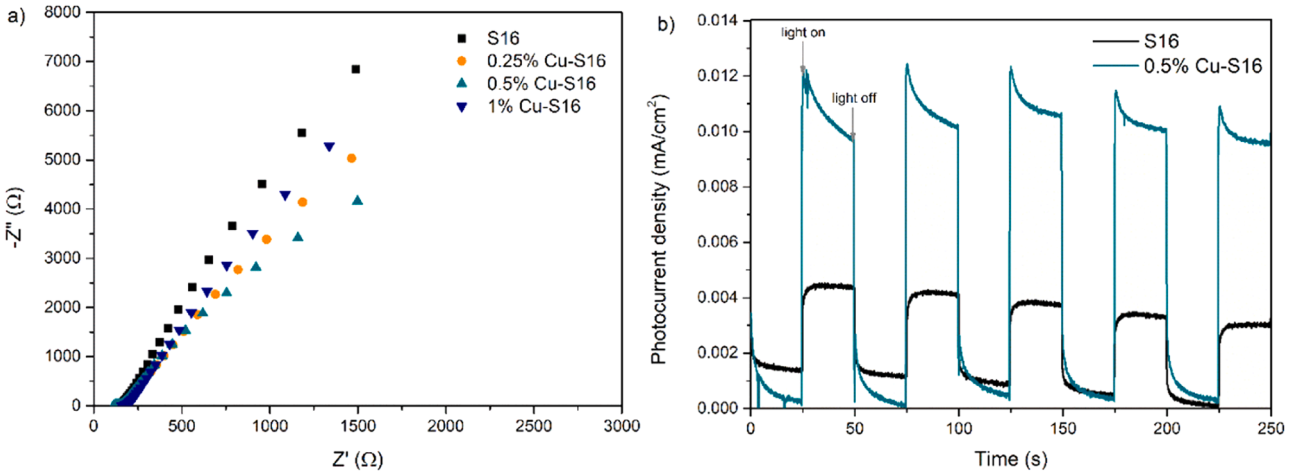

Fig. 11. EIS Nyquist plots (a) and photocurrent density (b) of prepared materials.

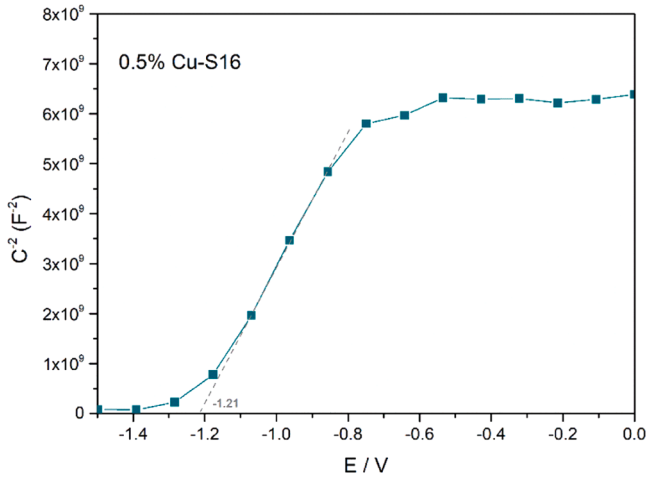

Fig. 12. Mott Schottky plot for 0.5% Cu-S16 composite.

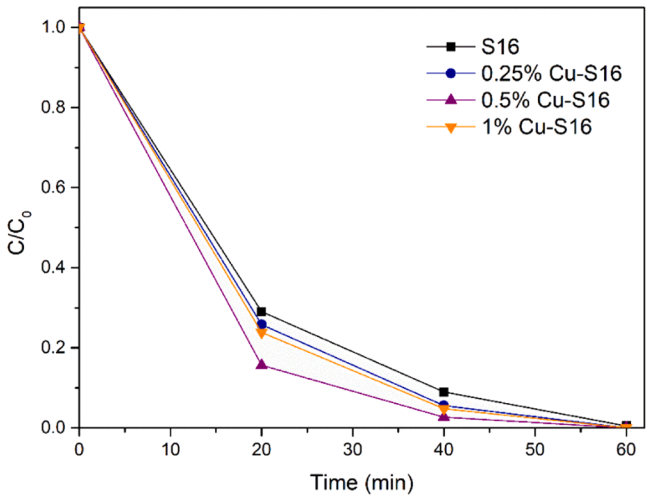

Fig. 13. CBZ degradation efficiency for samples modified with various copper amounts under UV–vis irradiation.

band, which is almost equal to the flat band potential for n-type semiconductors, was determined at − 1.21 V versus Ag and converted to − 0.41 V versus NHE.

Table 5
CBZ degradation rate constant and mineralisation measured as TOC removal efficiency.

Sample	CBZ degradation rate constant ($min^{-1} \cdot 10^{-2}$)	TOC removal (%)
Photolysis	0.2 ± 0.03	0
S16	6.6 ± 0.19	25.2
0.25% Cu-S16	7.2 ± 0.34	42.3
0.5% Cu-S16	9.0 ± 0.15	61.5
1% Cu-S16	7.6 ± 0.20	46.4
Photolysis + PMS	4.9 ± 0.17	2.1
S16 + PMS	8.3 ± 0.16	27.8
0.5% Cu-S16 + PMS	33.5 ± 1.54	65.3

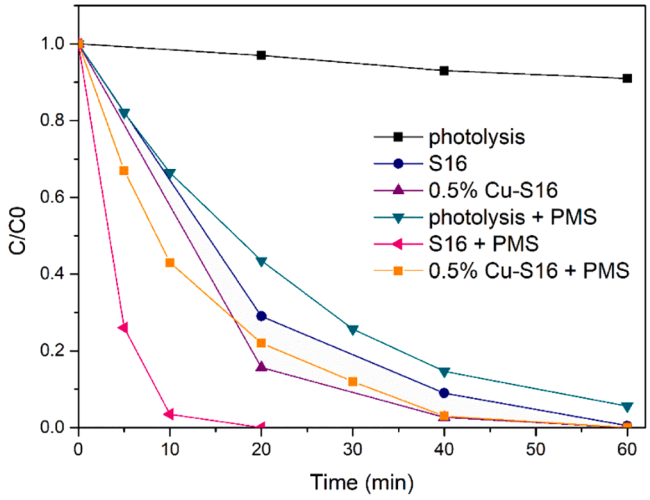

Fig. 14. CBZ degradation efficiency for processes with and without PMS addition.

The photocatalytic activity of the prepared samples was investigated in reaction of carbamazepine degradation, as presented in Fig. 13. Pure sample S16 (T220/EtOH-H_2O/17 h) synthesised under optimal conditions was compared with those modified with different amounts of copper from 0.25 wt% to 1 wt%. The incorporation of copper led to an increase in the photocatalytic activity of the composite. The optimal amount of copper was about 0.5 wt%. For this sample, 100% of CBZ was degraded within 60 min under simulated solar light. Compared with the S16 sample, the constant rate for the 0.5%-S16 sample increased from

MOST WIEDZY Downloaded from mostwiedzy.pl

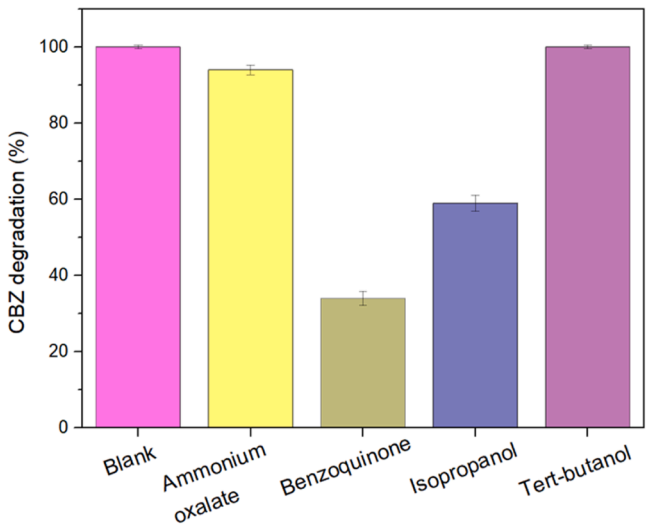

Fig. 15. Degradation of CBZ in the presence of scavengers for 0.5% Cu-S16/PMS.

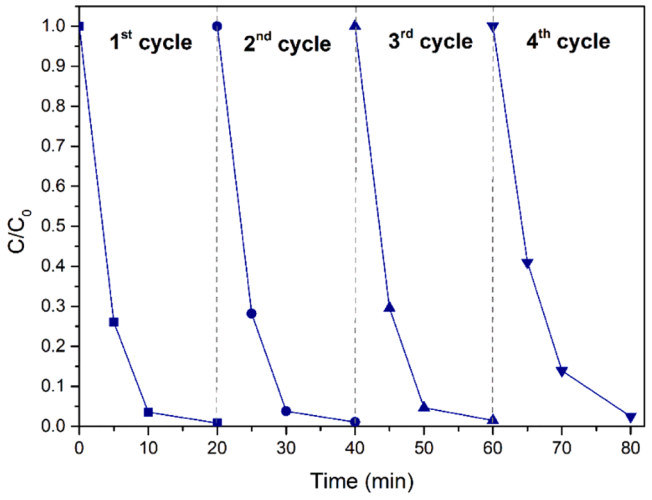

Fig. 16. CBZ degradation efficiency in the 4 subsequent cycles for 0.5% Cu-S16/PMS.

6.0 $min^{-1}\cdot10^{-2}$ to 9.0 $min^{-1}\cdot10^{-2}$ (see in Table 5). Moreover, the TOC removal efficiency increased from 25% to 61%.

In the next step, the photodegradation process in the presence of 0.5% Cu-S16 was combined with PMS activation. The results are shown in Fig. 14. It can be seen that PMS may be activated by light irradiation. The rate constant for photolysis with PMS increased from 0.2 $min^{-1}\cdot10^{-2}$ to 4.9 $min^{-1}\cdot10^{-2}$, compared with photolysis. A synergetic effect of the combination of the photocatalytic process and PMS activation for the degradation of CBZ was observed. The rate constant increased from 9.0 $min^{-1}\cdot10^{-2}$ for 0.5% Cu-S16 without PMS to 33.5 $min^{-1}\cdot10^{-2}$ for 0.5% Cu-S16 with PMS (Table 5). It can be explained by the fact that some transition metal ions, such as copper, can induce the generation of reactive sulphate radicals by coupling with PMS.

To verify the mechanism of CBZ degradation by 0.5% Cu-S16 in the presence of PMS, trapping experiments using radical scavengers were performed. As shown in Fig. 15, superoxide anion radicals ($\bullet O_2^-$) and sulphate radicals ($\bullet SO_4^-$) were the main reactive species involved in the efficient photodegradation process.

The stability and recyclability of the 0.5% Cu-S16/PMS system were evaluated in the four subsequent photodegradation cycles (Fig. 16). It can be observed that 0.5% Cu-S16/PMS may be effectively reusable, with nearly 100% degradation of CBZ within 20 min after the fourth cycle. Moreover, the XRD and FTIR analyses confirmed no changes in the material structure after the degradation processes (Fig. 17).

According to the Mott Schottky plot and band gap determined from the Kubelka Munk function, the conduction and valence bands were determined as − 0.41 V and 2.69 V, respectively. As presented in Fig. 18 the prepared photocatalyst can easily reduce oxygen to superoxide radicals (−0.18 V vs. NHE). According to XPS analysis, copper exists in two oxidation states: Cu(I) and Cu(II). Both of these species can activate PMS (Zhu et al., 2021). The following reactions may occur during PMS activation by Cu(II), which is considered a direct one-electron transfer reaction:

$$Cu^{2+} + HSO_5^- \rightarrow Cu^{3+} + \bullet SO_4^- + OH^- \quad (5)$$

Meanwhile, in the case of Cu(I), there are two possible routes: one-electron oxidation of Cu(I) or two-electron oxidation of Cu(I) to produce Cu(II) or Cu(III), respectively (Wang et al., 2020; Ding et al., 2022).

$$Cu^{+} + HSO_5^- \rightarrow Cu^{2+} + \bullet SO_4^- + OH^- \quad (6)$$

$$Cu^{+} + HSO_5^- \rightarrow Cu^{3+} + SO_4^{2-} + OH^- \quad (7)$$

Previous studies show that activating PMS using Cu (II) to generate ROS is difficult because this reaction is thermodynamically

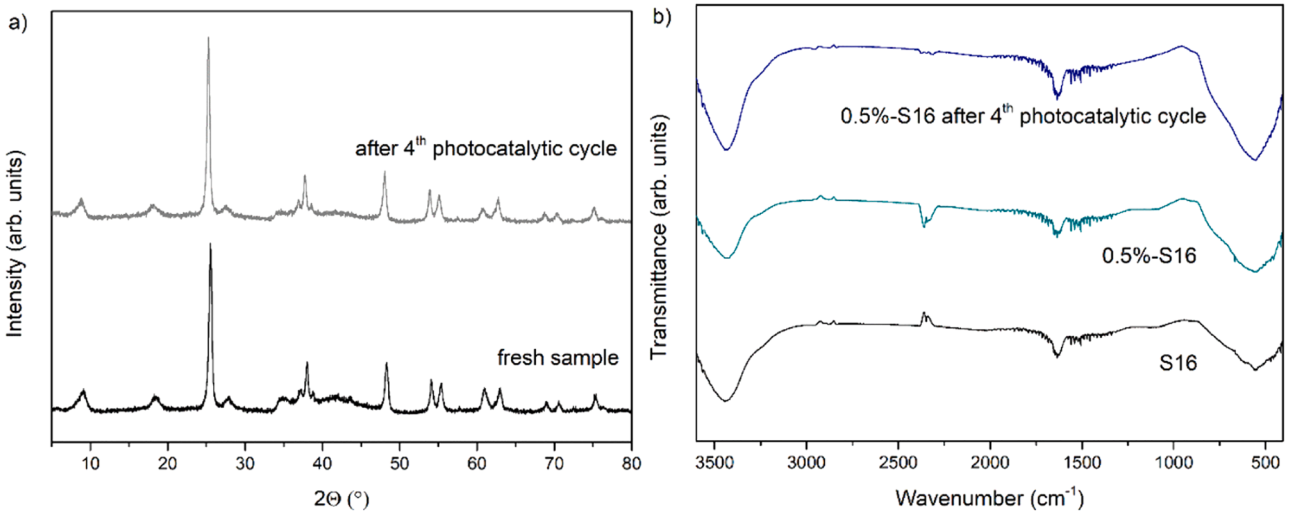

Fig. 17. The XRD diffractograms (a) and FTIR spectra (b) of fresh and used 0.5%Cu-S16 composites.

MOST WIEDZY Downloaded from mostwiedzy.pl

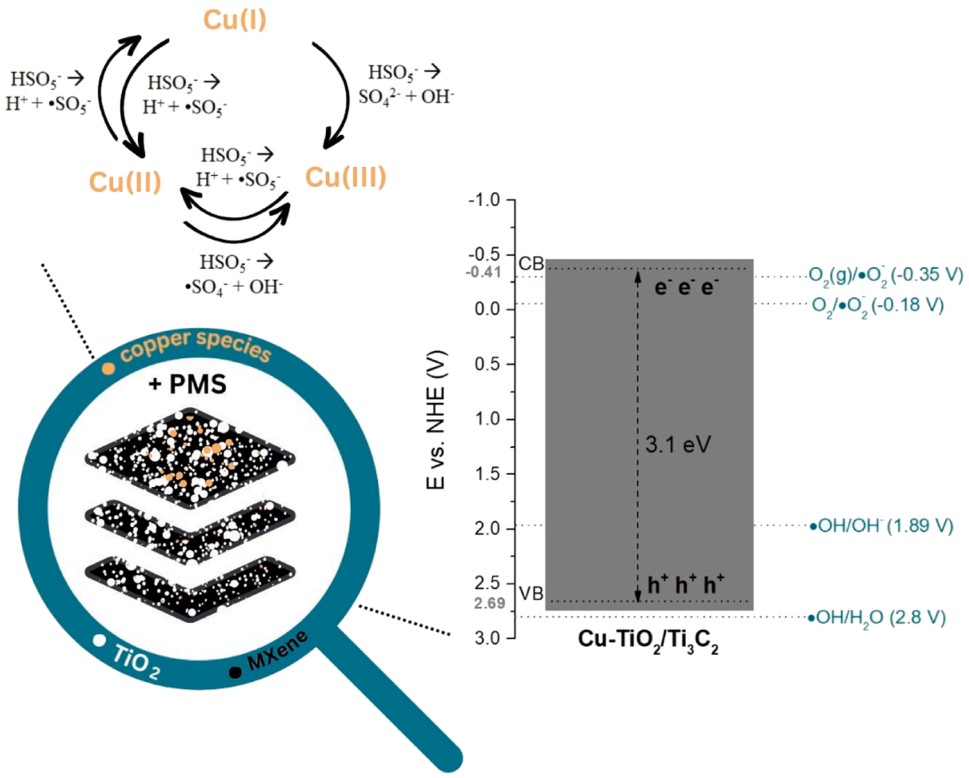

Fig. 18. Proposed scheme of degradation mechanism for the Cu-TiO_2/Ti_3C_2/PMS system.

unfavourable. Moreover, the degradation rate of pollutants by Cu(II) is slow, and the time is relatively long (Zhang et al., 2022). Furthermore, Cu(I) may effectively activate PMS to generate highly active radicals and promote the rapid decomposition of pollutants, owing to its stronger electron donation capacity.

5. Conclusions

In this work, the temperature, water/ethanol ratio, and hydrothermal reaction time were optimised using the Box- Behnken method to maximise carbamazepine photodegradation efficiency under simulated solar light. ANOVA was used to study the statistically significant parameters and their interactions. According to the RSM and ANOVA analyses, the optimum synthesis conditions were 220 °C, 17 h, and 58:42 v/v water/ethanol ratio, and the most important parameter affecting the synthesis of the highly photocatalytic active TiO_2/Ti_3C_2 composite material was the water/ethanol ratio. The optimised TiO_2/Ti_3C_2 sample exhibited the highest CBZ photodegradation efficiency, and complete CBZ degradation was observed within 60 min under simulated solar light irradiation.

Further analysis revealed that modification with copper species led to markedly improved photocatalytic activity, and the optimal copper content was 0.5 wt%. The combination of the photocatalytic process using the 0.5% Cu-S16 sample with PMS (0.5 mM) activation led to complete CBZ degradation within 20 min of irradiation under simulated solar light. The superoxide anion radicals and sulphate radicals were the main reactive species involved in the degradation process.

Declaration of Competing Interest

The authors declare that they have no known competing financial interests or personal relationships that could have appeared to influence the work reported in this paper.

Acknowledgements

The research was financially supported by Polish National Science Centre (Grant No. NCN 2021/43/B/ST5/02983).

Appendix A. Supporting information

Supplementary data associated with this article can be found in the online version at doi:10.1016/j.psep.2023.09.028.

References

Afreen, G., Shoeb, M., Upadhyayula, S., 2020. Effectiveness of reactive oxygen species generated from rGO/CdS QD heterostructure for photodegradation and disinfection of pollutants in waste water. Mater. Sci. Eng.: C. 108, 110372 https://doi.org/10.1016/j.msec.2019.110372.

Ahmed, B., Anjum, D.H., Hedhili, M.N., Gogotsi, Y., Alshareef, H.N., 2016. H_2O_2 assisted room temperature oxidation of Ti_2C MXene for Li-ion battery anodes. Nanoscale 8, 7580–7587. https://doi.org/10.1039/C6NR00002A.

Almeida, Â., Soares, A.M.M., Esteves, V.I., Freitas, R., 2021. Occurrence of the antiepileptic carbamazepine in water and bivalves from marine environments: a review. Environ. Toxicol. Pharm. 86, 103661 https://doi.org/10.1016/j.etap.2021.103661.

Asencios, Y.J.O., Lourenço, V.S., Carvalho, W.A., 2022. Removal of phenol in seawater by heterogeneous photocatalysis using activated carbon materials modified with TiO_2, 388–389 Catal. Today 247–258. https://doi.org/10.1016/j.cattod.2020.06.064.

Biesinger, M.C., Lau, L.W.M., Gerson, A.R., 2010. Resolving surface chemical states in XPS analysis of first row transition metals, oxides and hydroxides: Sc, Ti, V, Cu and Zn. Appl. Surf. Sci. 257, 887–898. https://doi.org/10.1016/j.apsusc.2010.07.086.

Danish, M.S.S., Estrella, L.L., Alemaida, I.M.A., Lisin, A., Moiseev, N., Ahmadi, M., Nazari, M., Wali, M., Zaheb, H., Senjyu, T., 2021. Photocatalytic applications of metal oxides for sustainable environmental remediation. Met. (Basel) 11, 80. https://doi.org/10.3390/met11010080.

Ding, X., Li, Y., Li, C., Wang, W., Wang, L., Feng, L., Han, D., 2019. 2D visible-light-driven TiO_2@Ti_3C_2/g-C_3N_4 ternary heterostructure for high photocatalytic activity. J. Mater. Sci. 54, 9385–9396. https://doi.org/10.1007/s10853-018-03289-4.

Ding, Y., Fu, L., Peng, X., Lei, M., Wang, C., Jiang, J., 2022. Copper catalysts for radical and nonradical persulfate based advanced oxidation processes: certainties and uncertainties. Chem. Eng. J. 427, 131776 https://doi.org/10.1016/j.cej.2021.131776.

MOST WIEDZY Downloaded from mostwiedzy.pl

Dong, H., Zeng, G., Tang, L., Fan, C., Zhang, C., He, X., He, Y., 2015. An overview on limitations of TiO_2-based particles for photocatalytic degradation of organic pollutants and the corresponding countermeasures. Water Res. 79, 128–146. https://doi.org/10.1016/j.watres.2015.04.038.

Dudziak, S., Kowalkińska, M., Karczewski, J., Pisarek, M., Siuzdak, K., Kubiak, A., Siwińska-Ciesielczyk, K., Zielińska-Jurek, A., 2021. Solvothermal growth of {0 0 1} exposed anatase nanosheets and their ability to mineralise organic pollutants. The effect of alcohol type and content on the nucleation and growth of TiO_2 nanostructures. Appl. Surf. Sci. 563, 150360 https://doi.org/10.1016/j.apsusc.2021.150360.

Gawande, M.B., Goswami, A., Felpin, F.X., Asefa, T., Huang, X., Silva, R., Zou, X., Zboril, R., Varma, R.S., 2016. Cu and Cu-based nanoparticles: synthesis and applications in catalysis. Chem. Rev. 116, 3722–3811. https://doi.org/10.1021/acs.chemrev.5b00482.

Grzegórska, A., Głuchowski, P., Karczewski, J., Ryl, J., Wysocka, I., Siuzdak, K., Trykowski, G., Grochowska, K., Zielińska-Jurek, A., 2021. Enhanced photocatalytic activity of accordion-like layered Ti_3C_2 (MXene) coupled with Fe-modified decahedral anatase particles exposing {1 0 1} and {0 0 1} facets. Chem. Eng. J. 426, 130801 https://doi.org/10.1016/j.cej.2021.130801.

Gubitosa, J., Mongiovi', C., Romita, R., Cosma, P., Nuzzo, S., Rizzi, V., Fini, P., 2022. Removal of emerging contaminants from water using cyclodextrin-based polymers and advanced oxidation processes: the case of carbamazepine. Processes 10, 1703. https://doi.org/10.3390/pr10091703.

Hai, F., Yang, S., Asif, M., Sencadas, V., Shawkat, S., Sanderson-Smith, M., Gorman, J., Xu, Z.Q., Yamamoto, K., 2018. Carbamazepine as a possible anthropogenic marker in water: occurrences, toxicological effects, regulations and removal by wastewater treatment technologies. Water (Basel) 10, 107. https://doi.org/10.3390/w10020107.

Hasija, V., Raizada, P., Thakur, V.K., Ahamad, T., Alshehri, S.M., Thakur, S., Nguyen, V. H., van Le, Q., Singh, P., 2022. An overview on photocatalytic sulfate radical formation via doped graphitic carbon nitride for water remediation. Curr. Opin. Chem. Eng. 37, 100841 https://doi.org/10.1016/j.coche.2022.100841.

Hua, Z., Dai, Z., Bai, X., Ye, Z., Wang, P., Gu, H., Huang, X., 2016. Copper nanoparticles sensitised TiO_2 nanotube arrays electrode with enhanced photoelectrocatalytic activity for diclofenac degradation. Chem. Eng. J. 283, 514–523. https://doi.org/10.1016/j.cej.2015.07.072.

Huang, W.X., Li, Z.P., Li, D.D., Hu, Z.H., Wu, C., Lv, K.L., Li, Q., 2022. Ti_3C_2 MXene: recent progress in its fundamentals, synthesis, and applications. Rare Met. 41, 3268–3300. https://doi.org/10.1007/s12598-022-02058-2.

Im, J.K., Sohn, E.J., Kim, S., Jang, M., Son, A., Zoh, K.D., Yoon, Y., 2021. Review of MXene-based nanocomposites for photocatalysis. Chemosphere 270, 129478. https://doi.org/10.1016/j.chemosphere.2020.129478.

Isac, L., Cazan, C., Andronic, L., Enesca, A., 2022. CuS-based nanostructures as catalysts for organic pollutants photodegradation. Catalysts 12, 1135. https://doi.org/10.3390/catal12101135.

Kalambate, P.K., Sinha Dhanjai, A., Li, Y., Shen, Y., Huang, Y., 2020. An electrochemical sensor for ifosfamide, acetaminophen, domperidone, and sumatriptan based on self-assembled MXene/MWCNT/chitosan nanocomposite thin film. Microchim. Acta 187, 402. https://doi.org/10.1007/s00604-020-04366-9.

Li, K., Jiao, T., Xing, R., Zou, G., Zhou, J., Zhang, L., Peng, Q., 2018. Fabrication of tunable hierarchical MXene@AuNPs nanocomposites constructed by self-reduction reactions with enhanced catalytic performances. Sci. China Mater. 61, 728–736. https://doi.org/10.1007/s40843-017-9196-8.

Li, X., Peng, W., Li, L., Chen, S., Ye, L., Peng, C., 2022. Simple synthesis of copper/MXene/polyacrylamide hydrogel catalyst for 4-nitrophenol reduction. Mater. Lett. 324, 132705 https://doi.org/10.1016/j.matlet.2022.132705.

Mezzelani, M., Fattorini, D., Gorbi, S., Nigro, M., Regoli, F., 2020. Human pharmaceuticals in marine mussels: evidence of sneaky environmental hazard along Italian coasts. Mar. Environ. Res. 162, 105137 https://doi.org/10.1016/j.marenvres.2020.105137.

Muscetta, M., Clarizia, L., Garlisi, C., Palmisano, G., Marotta, R., Andreozzi, R., di Somma, I., 2020. Hydrogen production upon UV-light irradiation of Cu/TiO2 photocatalyst in the presence of alkanol-amines. Int. J. Hydrog. Energy 45, 26701–26715. https://doi.org/10.1016/j.ijhydene.2020.07.002.

Rathi, B.S., Kumar, P.S., Show, P.L., 2021. A review on effective removal of emerging contaminants from aquatic systems: current trends and scope for further research. J. Hazard. Mater. 409, 124413 https://doi.org/10.1016/j.jhazmat.2020.124413.

Rivera-Utrilla, J., Sánchez-Polo, M., Ferro-García, M.Á., Prados-Joya, G., Ocampo-Pérez, R., 2013. Pharmaceuticals as emerging contaminants and their removal from water. A review. Chemosphere 93, 1268–1287. https://doi.org/10.1016/j.chemosphere.2013.07.059.

Shaaban, E., Li, G., 2022. Probing active sites for carbon oxides hydrogenation on Cu/TiO_2 using infrared spectroscopy. Commun. Chem. 5, 32 https://doi.org/10.1038/s42004-022-00650-2.

Shen, R., Xie, J., Guo, P., Chen, L., Chen, X., Li, X., 2018. Bridging the g-C_3N_4 nanosheets and robust CuS cocatalysts by metallic acetylene black interface mediators for active and durable photocatalytic H_2 production. ACS Appl. Energy Mater. 1, 2232–2241. https://doi.org/10.1021/acsaem.8b00311.

Simamora, A.J., Hsiung, T.L., Chang, F.C., Yang, T.C., Liao, C.Y., Wang, H.P., 2012. Photocatalytic splitting of seawater and degradation of methylene blue on CuO/nano TiO_2. Int. J. Hydrog. Energy 37, 13855–13858. https://doi.org/10.1016/j.ijhydene.2012.04.091.

Vattikuti, S.V.P., Reddy, P.A.K., Shim, J., Byon, C., 2018. Visible-light-driven photocatalytic activity of SnO_2 –ZnO quantum dots anchored on g-C_3N_4 nanosheets for photocatalytic pollutant degradation and H_2 production. ACS Omega 3, 7587–7602. https://doi.org/10.1021/acsomega.8b00471.

Verma, R., Gangwar, J., Srivastava, A.K., 2017. Multiphase TiO_2 nanostructures: a review of efficient synthesis, growth mechanism, probing capabilities, and applications in bio-safety and health. RSC Adv. 7, 44199–44224. https://doi.org/10.1039/C7RA06925A.

Wang, L., Xu, H., Jiang, N., Wang, Z., Jiang, J., Zhang, T., 2020. Trace cupric species triggered decomposition of peroxymonosulfate and degradation of organic pollutants: Cu(III) being the primary and selective intermediate oxidant. Environ. Sci. Technol. 54, 4686–4694. https://doi.org/10.1021/acs.est.0c00284.

Wang, Y., Zhao, P., Gao, B., Yuan, M., Yu, J., Wang, Z., Chen, X., 2023. Self-reduction of bimetallic nanoparticles on flexible MXene-graphene electrodes for simultaneous detection of ascorbic acid, dopamine, and uric acid. Microchem. J. 185, 108177 https://doi.org/10.1016/j.microc.2022.108177.

Wolski, L., Walkowiak, A., Ziolek, M., 2019. Formation of reactive oxygen species upon interaction of Au/ZnO with H_2O_2 and their activity in methylene blue degradation. Catal. Today 333, 54–62. https://doi.org/10.1016/j.cattod.2018.04.004.

Wu, L., Yue, X., Chang, Y., Wang, K., Zhang, J., Sun, J., Wei, Z., Kowalska, E., 2022. Photocatalytic degradation of tetracycline under visible light irradiation on $BiVO_4$ microballs modified with noble metals. Catalysts 12, 1293. https://doi.org/10.3390/catal12111293.

Yan, H., Zhao, T., Li, X., Hun, C., 2015. Synthesis of Cu-doped nano-TiO_2 by detonation method. Ceram. Int. 41, 14204–14211. https://doi.org/10.1016/j.ceramint.2015.07.046.

Zhang, B., Han, Z., Xin, Y., Zhang, Y., Li, W., Li, B., Ding, A., Ma, J., He, X., 2022. Peroxymonosulfate activation by vacuum ultraviolet and trace copper ions: a new way to boost Cu(II)/Cu(I) redox cycle. Chem. Eng. J. 450, 138097 https://doi.org/10.1016/j.cej.2022.138097.

Zhang, X., Liu, Y., Dong, S., Ye, Z., Guo, Y., 2017. One-step hydrothermal synthesis of a TiO_2-$Ti_3C_2T_x$ nanocomposite with small sized TiO_2 nanoparticles. Ceram. Int. 43, 11065–11070. https://doi.org/10.1016/j.ceramint.2017.05.151.

Zhang, Y., Geißen, S.U., Gal, C., 2008. Carbamazepine and diclofenac: removal in wastewater treatment plants and occurrence in water bodies. Chemosphere 73, 1151–1161. https://doi.org/10.1016/j.chemosphere.2008.07.086.

Zhang, Y.Z., El-Demellawi, J.K., Jiang, Q., Ge, G., Liang, H., Lee, K., Dong, X., Alshareef, H.N., 2020. MXene hydrogels: fundamentals and applications. Chem. Soc. Rev. 49, 7229–7251. https://doi.org/10.1039/D0CS00022A.

Zhang, Z., Li, H., Zou, G., Fernandez, C., Liu, B., Zhang, Q., Hu, J., Peng, Q., 2016. Self-reduction synthesis of new MXene/Ag composites with unexpected electrocatalytic activity. ACS Sustain Chem. Eng. 4, 6763–6771. https://doi.org/10.1021/acssuschemeng.6b01698.

Zhou, S., Zhao, Y., Shi, R., Wang, Y., Ashok, A., Héraly, F., Zhang, T., Yuan, J., 2022. Vacancy-rich MXene-immobilized Ni single atoms as a high-performance electrocatalyst for the hydrazine oxidation reaction. Adv. Mater. 34, 2204388 https://doi.org/10.1002/adma.202204388.

Zhu, J., Tang, Y., Yang, C., Wang, F., Cao, M., 2016. Composites of TiO_2 nanoparticles deposited on Ti_3C_2 MXene nanosheets with enhanced electrochemical performance. J. Electrochem Soc. 163, A785–A791. https://doi.org/10.1149/2.0981605jes.

Zhu, Y., Li, D., Zuo, S., Guan, Z., Ding, S., Xia, D., Li, X., 2021. Cu_2O/CuO induced non-radical/radical pathway toward highly efficient peroxymonosulfate activation. J. Environ. Chem. Eng. 9, 106781 https://doi.org/10.1016/j.jece.2021.106781.

Zind, H., Mondamert, L., Remaury, Q.B., Cleaon, A., Leitner, N.K.V., Labanowski, J., 2021. Occurrence of carbamazepine, diclofenac, and their related metabolites and transformation products in a French aquatic environment and preliminary risk assessment. Water Res 196, 117052. https://doi.org/10.1016/j.watres.2021.117052.

Zou, G., Zhang, Z., Guo, J., Liu, B., Zhang, Q., Fernandez, C., Peng, Q., 2016. Synthesis of MXene/Ag composites for extraordinary long cycle lifetime lithium storage at high rates. ACS Appl. Mater. Interfaces 8, 22280–22286. https://doi.org/10.1021/acsami.6b08089.

MOST WIEDZY Downloaded from mostwiedzy.pl